
This is an electronic reprint of the original article.
This reprint may differ from the original in pagination and typographic detail.

Okumura, Hironori; Suihkonen, Sami; Lemettinen, Jori; Uedono, Akira; Zhang, Yuhao; Piedra, Daniel; Palacios, Tomás

AlN metal-semiconductor field-effect transistors using Si-ion implantation

Published in:
Japanese Journal of Applied Physics

DOI:
[10.7567/JJAP.57.04FR11](https://doi.org/10.7567/JJAP.57.04FR11)

Published: 01/04/2018

Document Version
Peer-reviewed accepted author manuscript, also known as Final accepted manuscript or Post-print

Please cite the original version:
Okumura, H., Suihkonen, S., Lemettinen, J., Uedono, A., Zhang, Y., Piedra, D., & Palacios, T. (2018). AlN metal-semiconductor field-effect transistors using Si-ion implantation. *Japanese Journal of Applied Physics*, 57(4), Article 04FR11. <https://doi.org/10.7567/JJAP.57.04FR11>

This material is protected by copyright and other intellectual property rights, and duplication or sale of all or part of any of the repository collections is not permitted, except that material may be duplicated by you for your research use or educational purposes in electronic or print form. You must obtain permission for any other use. Electronic or print copies may not be offered, whether for sale or otherwise to anyone who is not an authorised user.

AlN metal-semiconductor field-effect transistors using Si-ion implantation

Hironori Okumura^{1,2*}, Sami Suihkonen³, Jori Lemettinen³, Akira Uedono¹, Yuhao Zhang², Daniel Piedra², and Tomás Palacios²

1 Faculty of Pure and Applied Science, University of Tsukuba, Tsukuba 305-8573 Japan

2 Department of Electrical Engineering and Computer Science, Massachusetts Institute of Technology, Cambridge, MA 02139 USA

3 Department of Electronics and Nano-engineering, Aalto University, Espoo 02150 Finland

*E-mail: okumura.hironori.gm@u.tsukuba.ac.jp

We report on the electrical characterization of Si-ion implanted AlN layers and the first demonstration of metal-semiconductor field-effect transistors (MESFETs) with an ion-implanted AlN channel. The ion-implanted AlN layers with Si dose of $5 \times 10^{14} \text{ cm}^{-2}$ exhibit *n*-type characteristics after thermal annealing at 1230°C. The ion-implanted AlN MESFETs provide good drain current saturation and stable pinch-off operation even at 250°C. The off-state breakdown voltage is 2370 V for drain-to-gate spacing of 25 μm . These results show the great potential of AlN-channel transistors for high-temperature and high-power applications.

1. Introduction

AlN is an attractive material for high-temperature and high-power applications due to its high critical electric field (E_c), high thermal conductivity of 320 W/mK at room temperature, and a band-gap energy of 6.1 eV.^{1,2)} Due to the limited availability of bulk AlN substrates, typical AlN layers are hetero-epitaxially grown by metal-organic chemical-vapor deposition (MOCVD) and molecular-beam epitaxy.^{3,4)} The use of high-temperature growth systems has helped to significantly improve the quality of AlN hetero-epitaxial layers,^{5,6)} which are now ready for device demonstration.

Baliga's figure of merit (FOM) is widely used to evaluate the suitability of semiconductor materials for power electronics. It is defined as $\varepsilon\mu E_c^3 / (\varepsilon\mu E_c^3)_{\text{Si}}$, where ε the permittivity and μ the carrier mobility. Baliga's FOM of AlN ($=1.5 \times 10^4$) is more than one order of magnitude higher than SiC ($=3.4 \times 10^2$) and GaN ($=1.5 \times 10^3$) primarily due to the high E_c in AlN.^{7,8)} Fig. 1 shows the theoretical limits for the specific on-resistance in unipolar power devices as a function of the breakdown voltage (V_{br}) for the major wide band-gap semiconductors. AlN power devices allow much lower on resistance in comparison with SiC and GaN devices, leading to the great potential for high-power and high-efficiency applications.

AlN has been used in barrier layers of GaN-based high-electron mobility transistors (HEMTs) in order to reduce AlGaIn-alloy scattering and to increase two-dimensional electron-gas density and confinement.^{9,10)} Recently, high Al-content AlGaIn-channel HEMTs have been investigated for high-temperature and high-power applications.^{11,12)} However, Schottky-barrier diodes and deep-ultraviolet light-emitting diodes are among the few AlN-channel devices reported in the literature so far.^{13,14)} Due to the lack of suitable higher band-gap materials for hetero-structures, polarization induced doping cannot be utilized to generate electron conduction in AlN. Thus, the formation of an AlN channel requires impurity-doped AlN layers.

The doping concentration in III-N semiconductors is controlled by impurity incorporation during crystal growth, thermal diffusion, and ion implantation. Direct doping during growth allows the semiconductors to keep high crystalline quality. Although Si is used as a n -type dopant in AlN, there are few reports on heavily Si-doped AlN growth.¹⁵⁻¹⁷⁾ The n -type AlN epitaxial layers are still obtained with difficulty. On the other hand, ion implantation enables the impurity incorporation into unintentional doped (UID) AlN layers, which are commercially available. High-dose and high-energy ions have been used in the past in III-N semiconductors to obtain a high carrier concentration at some-hundred-nm

depth.¹⁸⁻²⁰⁾ This high-dose and high-energy ion implantation significantly damages the crystal lattice and introduces a high concentration of point defects, resulting in carrier compensation. Thermal annealing is helpful to heal the ion-implantation damage, although very high temperatures are typically required in wide band-gap semiconductors (e.g. 900-1000°C for Ga₂O₃,²¹⁾ 1000-1400°C for AlGa_N,^{18-20,22)} and 1400-1700°C for SiC²³⁾) due to the high thermal stability of point defects. The Si-ion implantation damage in AlN can be healed by annealing for 1230-1600°C in a nitrogen ambient, showing *n*-type conductance.^{19,24)} Still, there is no report on the detailed electrical properties of an ion-implanted AlN layer. In this letter, we report on the electrical characterization of Si-ion implanted AlN layers and the demonstration of ion-implanted AlN metal-semiconductor field-effect transistors (MESFETs).

2. Si-ion implantation to AlN

2.1 Experimental procedure

We used 1- μ m-thick UID AlN templates grown on sapphire using MOCVD, which are supplied by DOWA Electronics Materials Co., Ltd. To form the transistor channel, Si ion was implanted on the as-grown wafer at room temperature. The amount and penetration depth of implanted ions are controlled by implantation dose and ion-beam energy, respectively. To create the desired box profile of dopants, the ion-beam energies of 90, 40, and 10 keV were chosen at a ratio of 64%, 24%, and 12% in total implantation dose, respectively. The Si implantations with various doses of 5×10^{14} - 1×10^{16} cm⁻² were performed for incident angles of 0 and 7° from [0001]. Under these implantation conditions, the SRIM (stopping and range of ions in matter) Monte-Carlo simulations show a resulting Si concentration, e.g., average Si concentration of 1×10^{20} cm⁻³ in a 200-nm-deep box profile for a total Si dose of 2×10^{15} cm⁻². The Si concentration in the AlN layers was experimentally determined using secondary-ion mass spectrometry (SIMS) performed by EAG laboratories.

2.2 Si-doping profile

As shown in Fig. 2 (a), the AlN layers implanted at the incident angle of 0° had smaller Si concentration than what the SRIM simulation predicted and a 1- μ m-deep tail of $\sim 10^{19}$ cm⁻³. The discrepancy between the SIMS results and SRIM simulation is caused by the channeling effect, which allows some of implanted ions to travel without significant scattering along [0001].²⁵⁾ On the other hand, the AlN layers implanted at the incident angle of 7° exhibited a relatively uniform Si concentration in a 100-nm-deep box profile, as shown in Fig. 2 (b),

indicating that the channeling effect was suppressed. The remained discrepancy between the SIMS results ($4 \times 10^{19} \text{ cm}^{-3}$) and SRIM simulation ($2\text{-}3 \times 10^{19} \text{ cm}^{-3}$) could be removed by further controlling the incident angle.²⁵⁾ From the SIMS data, the concentration of hydrogen, carbon, and oxygen in the AlN layers were 2×10^{17} , 1×10^{17} , and $1 \times 10^{18} \text{ cm}^{-3}$, respectively. Additionally, the Si distribution in the ion-implanted AlN layers after the thermal annealing at the temperature of 1400°C for 30 min in a nitrogen ambient, which is performed by Nisshin Ion Equipment Co., Ltd., is shown in Fig. 2 (b). Very limited Si diffusion was observed in the AlN layer under the thermal-annealing condition. This is in contrast with the large Si diffusion observed in GaN and Ga_2O_3 layers for temperatures $> 1100^\circ\text{C}$.^{21,22)}

2.3 Surface roughness

To heal the ion-implantation damage in AlN, thermal annealing was performed at heater temperatures of $1100\text{-}1500^\circ\text{C}$ for 30 min in a nitrogen ambient at 200 mbar using a high-temperature MOCVD reactor. The wafer/sample surface temperature was monitored by an *in-situ* optical pyrometer, e.g., $1160 \pm 20^\circ\text{C}$ and $1230 \pm 20^\circ\text{C}$ for a heater temperature of 1300°C and 1500°C , respectively. Using atomic force microscopy, we observed the surface morphologies of the ion-implanted AlN layers with Si dose of 5×10^{14} - $1 \times 10^{16} \text{ cm}^{-2}$ before and after annealing at the surface temperature of 1230°C . All AlN surfaces before and after ion-implantation had root-mean-square (RMS) roughness with 0.5 ± 0.2 and 0.6 ± 0.1 nm, respectively, for a $10 \times 10 \mu\text{m}^2$ scan.

After thermal annealing, the RMS-surface roughness of the ion-implanted AlN layers with a Si dose of $2 \times 10^{15} \text{ cm}^{-2}$ was 0.7 ± 0.1 nm, despite the fact that no cap layer was used to suppress the migration of surface atoms.^{26,27)} This highlights the excellent thermal stability of AlN at 1230°C in a nitrogen ambient. On the other hand, the AlN layers implanted with a Si dose of $1 \times 10^{16} \text{ cm}^{-2}$, or average Si concentration of $8 \times 10^{20} \text{ cm}^{-3}$, showed an RMS-surface roughness of 13 ± 2 nm after the thermal annealing. We believe that the high-dose implantation leads to broken Al-N bonds, which allowed more aluminum and nitrogen atoms to migrate to the surface during the thermal annealing, increasing surface roughness. Further investigations, such as transmission-electron microscopy and Rutherford backscattering spectroscopy, are necessary to clarify the detailed relation between the annealing temperature and ion-implantation damage in AlN.

3. Electrical property of Si-ion implanted AlN

3.1 Experimental procedures

Electrical properties of the ion-implanted AlN layers were investigated. After ion implantation and subsequent high temperature annealing, the fabrication process continued with an HCl dip for 1 min for surface cleaning. A Ti (20 nm)/Al (100 nm)/Ni (25 nm)/Au (50 nm) metal stack was deposited using an electron-beam evaporation for source/drain contacts, followed by annealing at 800°C for 30 s in a nitrogen ambient to form metal alloy. A 200-nm-deep mesa isolation was obtained by Cl₂-based reactive-ion etching. Breakdown-voltage measurements were performed using an Agilent B1505A power-device analyzer and a high-voltage Tesla probe station. During breakdown measurements, the devices were immersed in a Fluorinert FC-770 solution to avoid surface flashover.^{28,29)}

3.2 I-V characteristics

Two Ti/Al/Ni/Au contacts separated by a 4- μ m source-drain spacing (L_{sd}) were used for the measurements. We confirmed that the ion-implanted AlN layer was electrically isolated by the bottom UID AlN layer. We note that surface temperatures below 1160°C were not enough for electrical activation of the ion-implanted AlN layers, in good agreement with a previous report.¹⁹⁾

The current-voltage characteristics of the ion-implanted AlN layer annealed at 1230°C are shown in Fig. 3 (a). The ion-implanted AlN layers with Si doses $< 1 \times 10^{15} \text{ cm}^{-2}$ were electrically conductive at room temperature. The current showed a Schottky behavior due to high potential barrier at a metal-AlN interface, and was independent of L_{sd} , indicating the high contact resistivity. As the measurement temperature increases from room temperature to 250°C, the current significantly increased and showed the ohmic-like behavior at 250°C. We consider that thermally excited carrier tunnels through the effective thinner potential barrier at the metal/n-type AlN interface, reducing the contact resistance. To obtain an ohmic behavior, the elimination of surface oxidation and the further optimization of annealing temperature and metal-stack structures are necessary.^{24, 30, 31)}

The ion-implanted AlN layers with a high Si dose $> 2 \times 10^{15} \text{ cm}^{-2}$ were not electrically conductive even after further high temperature annealing at 1700°C for 60 min in a nitrogen ambient using a face-to-face annealing methods.⁶⁾ Previously the electrical activation ratio of ion-implanted GaN has been reported to increase with increasing Si dose because point defects and impurities incorporated during growth are dominant in carrier compensation.²²⁾ In contrast, the electrical activation ratio of ion-implanted Ga₂O₃ reduces with increasing Si dose due to increase of ion-implantation damages and limit of annealing temperature $< 1000^\circ\text{C}$.²¹⁾ The low electrical activation of ion-implanted AlN may result from high thermal stability of point defects generated by the Si-ion implantation as well as the low thermal

diffusion of Si.

3.3 Electrical activation ratio

Hall-effect measurements at room temperature were performed on AlN samples, which were implanted with a Si dose of $5 \times 10^{14} \text{ cm}^{-2}$ at the incident angle of 7° , over an area of $200 \times 200 \text{ }\mu\text{m}^2$ using clover-leaf patterns. The electron mobility and sheet carrier concentration of the 100-nm-thick *n*-type AlN layer were $130 \text{ cm}^2/\text{Vs}$ and $6 \times 10^8 \text{ cm}^{-2}$, respectively. The electrical activation ratio, which is defined by the ratio of sheet-electron concentration to dopant dose, is 1×10^{-6} . In a previous report,¹⁹⁾ the electrical-activation ratio of Si-ion implanted AlN annealed at 1400°C for 10 min is estimated from the layer thickness of 200 nm, electron concentration of $2 \times 10^{15} \text{ cm}^{-3}$, and Si dose of $5 \times 10^{15} \text{ cm}^{-2}$ to be 8×10^{-6} , which is slightly higher than our results due to higher temperature annealing. The above activation ratios do not take into account the ionization energy (E_d) of the donor. Wide bandgap semiconductors have a large difference between electron and donor concentrations due to the high E_d (AlN: 0.2-0.3 eV for Si).^{7,17,32)} Despite low Si-donor concentration of $3 \times 10^{17} \text{ cm}^{-3}$, the electron concentration in the AlN layers doped during growth is $7 \times 10^{14} \text{ cm}^{-3}$ at room temperature,⁷⁾ which is higher than that in our Si-implanted AlN layers. This means that most of the Si atoms in the Si⁺-implanted AlN layers are not incorporated into the donor site or the implantation damage still remains. Higher annealing temperature and longer annealing time are expected to further increase the electron concentration.²⁴⁾

3.4 Two-terminal breakdown voltages

In the 200-nm-deep recess structure, lateral V_{br} of the UID AlN buffer layer was measured between the isolated source and drain contacts. The two-terminal V_{br} for various L_{sd} at room temperature are shown in Fig. 3 (b). For $L_{sd} < 10 \text{ }\mu\text{m}$, V_{br} increased linearly with increasing L_{sd} . For $L_{sd} > 10 \text{ }\mu\text{m}$, the breakdown saturated $2.5 \pm 0.3 \text{ kV}$. The effective critical electric field of the UID AlN buffer layer is 3.1 MV/cm , which is much higher than the one typically seen in the GaN and $\text{Al}_{0.1}\text{Ga}_{0.9}\text{N}$ buffer layers.^{33,34)} This experimentally shows that an AlN material has superior potential for high-power applications.

4. AlN MESFETs

4.1 Experimental procedures

AlN MESFETs were fabricated using AlN layers implanted with a Si dose of $5 \times 10^{14} \text{ cm}^{-2}$ at an incident angle of 7° , i.e., average Si concentration of $4 \times 10^{19} \text{ cm}^{-3}$ in the 100-nm depth, and thermally annealed at 1230°C . The structure of the fabricated AlN MESFETs is shown

in Fig. 4 (a). In addition to the recess process mentioned above, a Ni (30 nm)/Au (200 nm) metal stack was deposited for the gate electrode. The MESFETs had a gate length (L_g) of 2 μm and gate-source spacing (L_{gs}) of 2 μm .

4.2 Output/transfer characteristics

Output characteristics at room temperature for the MESFETs with L_{dg} of 4 μm are shown in Fig. 4 (b). The AlN MESFETs have a normally-on operation and pinch-off characteristics for gate voltage (V_{gs}) < -10 V. The subthreshold swing was 1.3 V/decade. Drain current (I_d) is effectively modulated by V_{gs} and shows good saturation. The maximum I_d was 8.7 $\mu\text{A}/\text{mm}$ for $V_{gs} = +8$ V. Output characteristics of the AlN MESFETs at 250°C are shown in Fig. 4 (c). Neither breakdown events nor other irreversible degradation was observed for $V_{ds} < +40$ V, suggesting a stable device operation in the whole temperature range from 25°C to 250°C. Both I_d and gate current increased with measurement temperature.

The transfer characteristics for the AlN MESFET with L_{gd} of 4 μm at a drain-voltage (V_{ds}) = +40 V at room temperature and 250°C are shown in Fig. 4 (d). At room temperature, the off-state I_d was 25 nA/mm, which is comparable with the gate current, indicating a negligibly-small leakage current through the UID AlN layers. The I_d on/off ratio was above 100. At 250°C, the off-state I_d and the I_d on/off ratio was 70 nA/mm and above 1000, respectively. The maximum transconductance at room temperature and 250°C was 0.7 and 23 $\mu\text{S}/\text{mm}$, respectively. Although the saturation I_d of typical Si and GaAs FETs reduce with increasing the measurement temperature due to the reduced mobility and saturation velocity, the performance of the AlN MESFETs significantly improved with increasing the temperature. We suggest that the limited I_d on/off ratio and transconductance of the AlN MESFETs arise from the high source/drain contact resistances and the high ionization energy of a Si donor as well as the low carrier concentration in the Si-ion implanted AlN.

4.3 Three-terminal breakdown voltages

For the AlN MESFETs with L_{gd} of 4 μm , the three-terminal V_{br} for $V_{gs} = -30$ V at room temperature and 250°C was 510 and 410 V, respectively. The three-terminal V_{br} for various L_{gd} at room temperature are shown in Fig. 5 (a). V_{br} increases linearly with increasing L_{gd} , achieving the maximum three-terminal V_{br} of 2370 V at $L_{gd} = 25$ μm .

The V_{br} characteristics for the AlN MESFETs with L_{gd} of 25 μm at room temperature are shown in Fig. 5 (b). The leakage current of off-state I_d was 60 nA/mm at -2000 V, which is much smaller than that some $\mu\text{A}/\text{mm}$ at -1000 V for GaN HEMTs.^{34,35} This small leakage current at a high reverse bias is advantageous for high-power applications.

For the ion-implanted AlN layer, the effective critical electric field of the three terminal V_{br} is 1.0 MV/cm, which is higher than that of GaN HEMTs due to high E_c of AlN.^{28,33,34)} AlGaIn HEMTs with a field plate have shown an effective critical electric field as high as 1.7 MV/cm thanks to reduction of the peak electric field at a gate edge.³⁶⁾ Further high breakdown voltages of the AlN MESFETs are expected in devices with a field-plate structure.

5. Conclusions

We report on the electrical characteristics of Si-ion implanted AlN and demonstration of an ion-implanted AlN MESFETs. The ion-implanted AlN layers with Si dose of 5×10^{14} cm⁻² exhibited *n*-type characteristics after thermal annealing at 1230°C in a nitrogen ambient, showing the sheet carrier concentration of 6×10^8 cm⁻² and the electron mobility of 130 cm²/Vs. The ion-implanted AlN MESFETs with a gate length of 2 μm have a maximum drain current of 8.7 μA/mm for gate voltage of +8 V and an on/off current ratio over 100 at room temperature. The AlN MESFETs can be further improved by reduction of the source/drain contact resistances and increase of the carrier concentrations in the AlN channel layer. At 250°C, excellent transistor pinch-off is achieved without permanent degradation. The maximum three-terminal off-state breakdown voltage is 2370 V for drain-to-gate spacing of 25 μm. The AlN-channel transistors show promise as high-temperature and high-power devices.

Acknowledgments

This work was supported by JSPS KAKENHI Grant No. 16H06424 and 17K14110, and the ONR PECASE program, monitored by Dr. Paul Maki. S. Suihkonen and J. Lemettinen acknowledge the financial support of the Academy of Finland (grant 297916) and the Foundation for Aalto University Science and Technology. A part of the research was performed at the OtaNano - Micronova Nanofabrication Centre of Aalto University. This work was carried out in part through the use of MIT's Microsystems Technology Laboratories and was partially supported for thermal annealing by TNSC.

References

- 1) G.A. Slack, R.A. Tanzilli, R.O. Pohl, and J.W. Vandersande, *J. Phys. Chem. Solids* **48**, 641 (1987).
- 2) H. Morkoc, "*Nitride Semiconductor Devices*", (Wiley-VCH, Germany, 2013).
- 3) M. Imura, H. Sugimura, N. Okada, M. Iwaya, S. Kamiyama, H. Amano, I. Akasaki, and A. Bandoh, *J. Cryst. Growth* **310**, 2308 (2008).
- 4) H. Okumura, T. Kimoto, and J. Suda, *Appl. Phys. Exp.* **4**, 025502 (2011).
- 5) A. Akanakova, D. Nilsson, and E. Janzen, *J. Cryst. Growth* **338**, 52 (2012).
- 6) H. Miyake, C. Lin, K. Tokoro, and K. Hiramatsu, *J. Cryst. Growth* **456**, 155 (2016).
- 7) Y. Taniyasu, M. Kasu, and T. Makimoto, *Appl. Phys. Lett.* **89**, 182112 (2006).
- 8) M. Higashiwaki, K. Sasaki, A. Kuramata, T. Masui, and S. Yamakoshi, *Appl. Phys. Lett.* **100**, 013504 (2012).
- 9) G. Li, R. Wang, J. Guo, J. Verma, Z. Hu, Y. Yue, F. Faria, Y. Cao, M. Kelly, T. Kosel, H. Xing, and D. Jena, *IEEE Electron Device Lett.* **33**, 661 (2012).
- 10) M. Qi, G. Li, S. Ganguly, P. Zhao, Z. Yan, J. Verma, B. Song, M. Zhu, K. Nomoto, H. Xing, and D. Jena, *Appl. Phys. Lett.* **110**, 063501 (2017).
- 11) H. Tokuda, M. Hatano, N. Yafune, S. Hashimoto, K. Akita, Y. Yamamoto, and M. Kuzuhara, *Appl. Phys. Exp.* **3**, 121003 (2010).
- 12) A. Baca, A. M. Armstrong, A. A. Allerman, E. A. Douglas, C. A. Sanchez, M. P. King, M. E. Coltrin, T. R. Fortune, and R. J. Kaplar, *Appl. Phys. Lett.* **109**, 033509 (2016).
- 13) Y. Taniyasu, M. Kasu, and T. Makimoto, *Nature* **441**, 325 (2006).
- 14) T. Kinoshita, T. Nagashima, T. Obata, S. Takashima, R. Yamamoto, R. Togashi, Y. Kumagai, R. Schlessler, R. Collazo, A. Koukitu, and Z. Sitar, *Appl. Phys. Exp.* **8**, 061003 (2015).
- 15) Y. Taniyasu, M. Kasu, and N. Kobayashi, *Appl. Phys. Lett.* **81**, 1255 (2002).
- 16) M. Hermann, F. Furtmayr, A. Bergmaier, G. Dollinger, M. Stuzmann, and M. Eickhoff, *Appl. Phys. Lett.* **86**, 192108 (2005).
- 17) S. B. Thapa, J. Hertkorn, F. Scholz, G. M. Prinz, R.A.R. Leute, M. Feneberg, K. Thonke, R. Sauer, O. Klein, J. Biskupek, and U. Kaiser, *J. Cryst. Growth* **310**, 4939 (2008).
- 18) S.O. Kucheyev, J.S. Williams, and S.J. Pearton, *Mat. Sci. and Eng. R* **33**, 51 (2001).
- 19) M. Kanechika and T. Kachi, *Appl. Phys. Lett.* **88**, 202106 (2006).
- 20) E.A. Moore, Y.K. Yeo, M.Y. Ryu, and R.L. Hengehold, *J. Electronic Materials* **38**, 153 (2009).
- 21) K. Sasaki, M. Higashiwaki, A. Kuramata, T. Masui, and S. Yamakoshi, *Appl. Phys. Exp.* **6**, 086502 (2013).

- 22) J. C. Zopler, H. H. Tan, J. S. Williams, J. Zou, D. J. H. Cockayne, S. J. Pearton, M. H. Crawford, and R. F. Karliceck, *Appl. Phys. Lett.* **70**, 2729 (1997).
- 23) T. Kimoto, A. Itoh, H. Matsunami, T. Nakata, and M. Watanabe, *J. Electronic Materials* **25**, 879 (1996).
- 24) H. Okumura, S. Suihkonen, J. Lemettinen, A. Uedono, and T. Palacios, *International Conference on Solid State Devices and Materials N-2-06*, 641 (2017).
- 25) T. Kimoto and J. A. Cooper, "*Fundamental of Silicon Carbide Technology: Growth, Characterization, Devices, and Applications*", (Willey, 2014)
- 26) G. J. Phelps, N. G. Wright, E. G. Chester, C. M. Johnson, A. G. O'Neil, S. Ortolland, A. Horsfall, K. Vassilevski, R. M. Gwilliam, P. G. Coleman, and C. P. Burrows, *Appl. Phys. Lett.* **80**, 228 (2002).
- 27) J.C. Zolper, D. J. Rieger, A. G. Baca, S. J. Pearton, J. W. Lee, and R. A. Stall, *Appl. Phys. Lett.* **69**, 538 (1996).
- 28) Y. Dora, A. Chakraborty, L. McCarthy, S. Keller, S. P. DenBaars, and U. K. Mishra, *IEEE Elect. Device Lett.* **27**, 713 (2006).
- 29) N. Tipirneri, A. Koudymov, V. Adivarihan, J. Yang, G. Simin, and M. A. Khan, *IEEE Elect. Device Lett.* **27**, 716 (2006).
- 30) N. Yafune, S. Hashimoto, K. Akita, Y. Yamamoto, and M. Kuzuhara, *Jpn. J. Appl. Phys.* **50**, 100202 (2011).
- 31) S. Bajaj, D. Akyol, S. Krishnamoorthy, Y. Zhang, and S. Rajan, *Appl. Phys. Lett.* **109**, 133508 (2016).
- 32) S. M. Sze and Kwok K. NG, "*Physics of Semiconductor Devices*", 3rd ed. (Wiley, New York, 1981).
- 33) B. Lu and T. Palacios, *IEEE Elect. Device Lett.* **31**, 951 (2010).
- 34) H. Lee, D. Piedra, M. Sun, X. Gao, S. Guo, and T. Palacios, *IEEE Elect. Device Lett.* **33**, 982 (2012)
- 35) S. Selvaraj, A. Watanabe, A. Wakejima, and T. Egawa, *IEEE Elect. Device Lett.* **33**, 1375 (2012)
- 36) T. Nanjo, A. Imai, Y. Suzuki, Y. Abe, T. Oishi, M. Suita, E. Yagyu, and Y. Tokuda, *IEEE Trans. Elect. Devices* **60**, 1046 (2013).

Figure Captions

Fig. 1. Relation between specific on-resistance and breakdown voltage of major wide band-gap semiconductors. The parameters used for these calculations are as follows. The permittivity ϵ are $11.8\epsilon_0$ for Si, $9.7\epsilon_0$ for SiC, $9.0\epsilon_0$ for GaN, $10\epsilon_0$ for Ga_2O_3 , $9.2\epsilon_0$ for AlN, and $5.5\epsilon_0$ for diamond. The mobility μ are $1400 \text{ cm}^2/\text{Vs}$ for Si, $1000 \text{ cm}^2/\text{Vs}$ for SiC, $2000 \text{ cm}^2/\text{Vs}$ for GaN, $300 \text{ cm}^2/\text{Vs}$ for Ga_2O_3 , $425 \text{ cm}^2/\text{Vs}$ for AlN, and $2000 \text{ cm}^2/\text{Vs}$ for diamond. The critical electric field E_c are 0.3 MV/cm for Si, 2.5 MV/cm for SiC, 3.3 MV/cm for GaN, 8.0 MV/cm for Ga_2O_3 , 12 MV/cm for AlN, and 10 MV/cm for diamond.^{7,8)}

Fig. 2. SIMS profile of Si concentration in Si-ion implanted AlN before thermal annealing (black solid line) and after thermal annealing at 1400°C (red solid line). Total Si doses of (a) $2 \times 10^{15} \text{ cm}^{-2}$ at incident angle of 0° and (b) $5 \times 10^{14} \text{ cm}^{-2}$ at incident angle of 7° were introduced using multiple-energy ion implantation. The results of the SRIM simulations are also shown (dash line).

Fig. 3. (a) Current-voltage characteristics of ion-implanted AlN with a Si dose of $5 \times 10^{14} \text{ cm}^{-2}$ (solid) and $1 \times 10^{16} \text{ cm}^{-2}$ (dash) between room temperature and 250°C . The inset shows the device pattern with contacts of $50 \mu\text{m} \times 100 \mu\text{m}$ rectangular shape. (b) Two-terminal buffer-leakage breakdown voltage as a function of source-to-drain spacing. The inset shows the measurement configuration of 200-nm-deep recess. Black dash line is fitted within $L_{sd} < 10 \mu\text{m}$ for the two-terminal breakdown voltage for various source-to-drain spacing of ion-implanted AlN on sapphire, while blue and purple dash lines are fitted within $L_{sd} < 30 \mu\text{m}$ for that in $\text{Al}_{0.1}\text{Ga}_{0.9}\text{N}$ on SiC and GaN on SiC.^{33,34)}

Fig. 4. (a) Schematic cross section of AlN MESFETs by Si-ion implantation. (b) DC output characteristics of ion-implanted AlN MESFET with gate length of $2 \mu\text{m}$ at room temperature for V_{gs} from -10 to $+8 \text{ V}$. (c) DC output characteristics of ion-implanted AlN MESFET with gate length of $2 \mu\text{m}$ at 250°C for V_{gs} from -8 to $+4 \text{ V}$. (d) Transfer characteristics at a drain voltage of $+40 \text{ V}$ at room temperature and 250°C .

Fig. 5. (a) Off-state breakdown characteristics of ion-implanted AlN MESFET with drain-

to-gate spacing of 25 μm at gate voltage of -30 V at room temperature. (b) Three-terminal off-state breakdown voltage as a function of gate-to-drain spacing at room temperature.

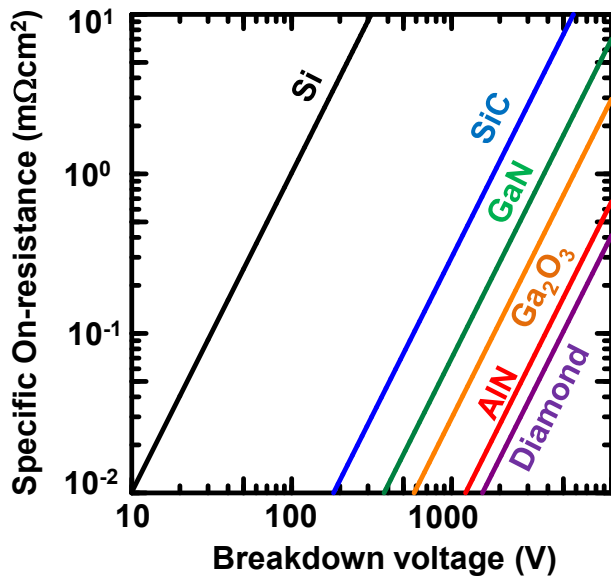


Fig. 1.

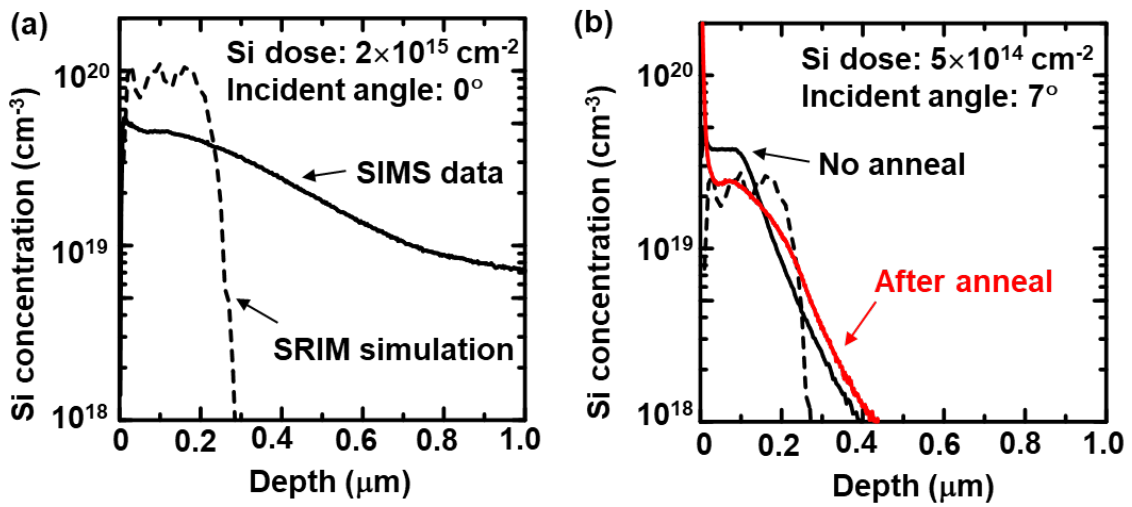


Fig. 2.

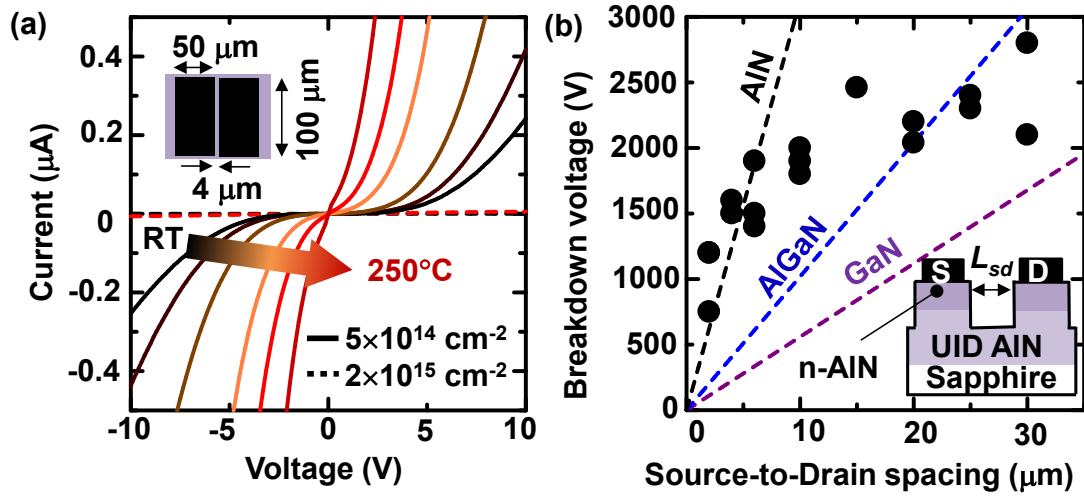


Fig. 3.

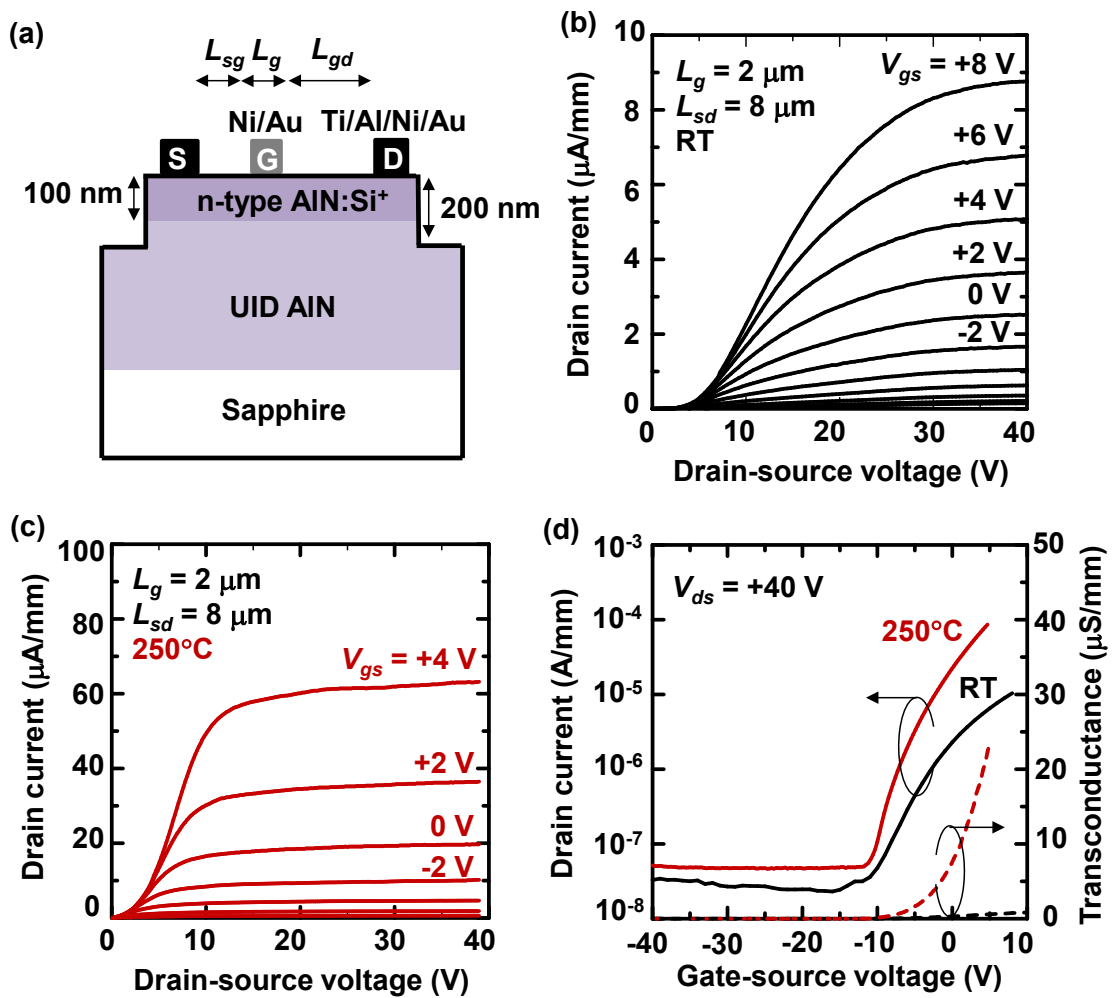


Fig. 4.

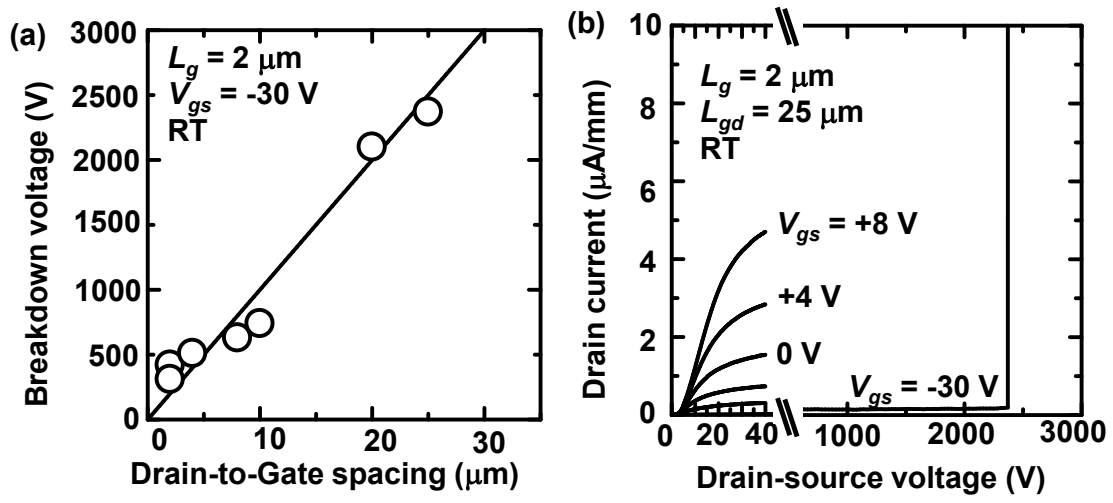


Fig. 5.